

Improved search for invisible modes of nucleon decay in water with the SNO+ detector

A. Allega,¹ M. R. Anderson,¹ S. Andringa,² M. Askins,^{3,4} D. J. Auty,⁵ A. Bacon,⁶ N. Barros,^{2,7} F. Barão,^{2,8} R. Bayes,⁹ E. W. Beier,⁶ T. S. Bezerra,¹⁰ A. Bialek,^{11,9} S. D. Biller,¹² E. Blucher,¹³ E. Caden,^{11,9} E. J. Callaghan,^{3,4} S. Cheng,¹ M. Chen,¹ O. Chkvorets,⁹ B. Cleveland,^{11,9} D. Cookman,¹² J. Corning,¹ M. A. Cox,^{14,2} R. Dehghani,¹ C. Deluce,⁹ M. M. Depatie,^{9,1} J. Dittmer,¹⁵ K. H. Dixon,¹⁶ F. Di Lodovico,¹⁶ E. Falk,¹⁰ N. Fatemighomi,¹¹ R. Ford,^{11,9} K. Frankiewicz,¹⁷ A. Gaur,⁵ O. I. González-Reina,¹⁸ D. Gooding,¹⁷ C. Grant,¹⁷ J. Grove,^{9,1} A. L. Hallin,⁵ D. Hallman,⁹ J. Hartnell,¹⁰ W. J. Heintzelman,⁶ R. L. Helmer,¹⁹ J. Hu,⁵ R. Hunt-Stokes,¹² S. M. A. Hussain,⁹ A. S. Inácio,^{2,7} C. J. Jillings,^{11,9} T. Kaptanoglu,^{3,4} P. Khaghani,⁹ H. Khan,⁹ J. R. Klein,⁶ L. L. Kormos,²⁰ B. Krar,¹ C. Kraus,^{9,11} C. B. Krauss,⁵ T. Kroupová,⁶ I. Lam,¹ B. J. Land,⁶ I. Lawson,^{11,9} L. Lebanowski,⁶ J. Lee,¹ C. Lefebvre,¹ J. Lidgard,¹² Y. H. Lin,^{9,1} V. Lozza,^{2,7} M. Luo,⁶ A. Maio,^{2,7} S. Manecki,^{11,1} J. Maneira,^{2,7} R. D. Martin,¹ N. McCauley,¹⁴ A. B. McDonald,¹ M. Meyer,¹⁵ C. Mills,¹⁰ I. Morton-Blake,¹² S. Naugle,⁶ L. J. Nolan,²¹ H. M. O’Keeffe,²⁰ G. D. Orebi Gann,^{3,4} J. Page,¹⁰ W. Parker,¹² J. Paton,¹² S. J. M. Peeters,¹⁰ L. Pickard,²² P. Ravi,⁹ A. Reichold,¹² S. Riccetto,¹ R. Richardson,⁹ M. Rigan,¹⁰ J. Rose,¹⁴ J. Rumleskie,⁹ I. Semeneč,¹ P. Skensved,¹ M. Smiley,^{3,4} R. Svoboda,²² B. Tam,¹ J. Tseng,¹² E. Turner,¹² S. Valder,¹⁰ J. G. C. Veinot,²³ C. J. Virtue,⁹ E. Vázquez-Jáuregui,¹⁸ J. Wang,¹² M. Ward,¹ J. J. Weigand,²⁴ J. D. Wilson,⁵ J. R. Wilson,¹⁶ A. Wright,¹ J. P. Yanez,⁵ S. Yang,⁵ M. Yeh,²⁵ S. Yu,⁹ T. Zhang,²² Y. Zhang,⁵ K. Zuber,^{15,26} and A. Zummo⁶

(The SNO+ Collaboration)

¹Queen’s University, Department of Physics, Engineering Physics & Astronomy, Kingston, Ontario K7L 3N6, Canada

²Laboratório de Instrumentação e Física Experimental de Partículas (LIP),
Av. Prof. Gama Pinto, 2, 1649-003, Lisboa, Portugal

³University of California, Berkeley, Department of Physics, California 94720, Berkeley, USA

⁴Lawrence Berkeley National Laboratory, 1 Cyclotron Road, Berkeley, California 94720-8153, USA

⁵University of Alberta, Department of Physics, 4-181 CCIS, Edmonton, Alberta T6G 2E1, Canada

⁶University of Pennsylvania, Department of Physics & Astronomy,
209 South 33rd Street, Philadelphia, Pennsylvania 19104-6396, USA

⁷Universidade de Lisboa, Faculdade de Ciências (FCUL),
Departamento de Física, Campo Grande, Edifício C8, 1749-016 Lisboa, Portugal

⁸Universidade de Lisboa, Instituto Superior Técnico (IST),

Departamento de Física, Av. Rovisco Pais, 1049-001 Lisboa, Portugal

⁹Laurentian University, Department of Physics, 935 Ramsey Lake Road, Sudbury, Ontario P3E 2C6, Canada

¹⁰University of Sussex, Physics & Astronomy, Pevensey II, Falmer, Brighton, BN1 9QH, United Kingdom

¹¹SNOLAB, Creighton Mine #9, 1039 Regional Road 24, Sudbury, Ontario P3Y 1N2, Canada

¹²University of Oxford, The Denys Wilkinson Building,
Keble Road, Oxford, OX1 3RH, United Kingdom

¹³The Enrico Fermi Institute and Department of Physics,
The University of Chicago, Chicago, Illinois 60637, USA

¹⁴University of Liverpool, Department of Physics, Liverpool, L69 3BX, United Kingdom

¹⁵Technische Universität Dresden, Institut für Kern und Teilchenphysik, Zellescher Weg 19, Dresden, 01069, Germany

¹⁶King’s College London, Department of Physics,

Strand Building, Strand, London, WC2R 2LS, United Kingdom

¹⁷Boston University, Department of Physics, 590 Commonwealth Avenue, Boston, MA 02215, USA

¹⁸Universidad Nacional Autónoma de México (UNAM),

Instituto de Física, Apartado Postal 20-364, México D.F., 01000, México

¹⁹TRIUMF, 4004 Wesbrook Mall, Vancouver, British Columbia V6T 2A3, Canada

²⁰Lancaster University, Physics Department, Lancaster, LA1 4YB, United Kingdom

²¹Queen Mary, University of London, School of Physics and Astronomy,
327 Mile End Road, London, E1 4NS, United Kingdom

²²University of California, Davis, 1 Shields Avenue, Davis, California 95616, USA

²³University of Alberta, Department of Chemistry,

11227 Saskatchewan Drive, Edmonton, Alberta, T6G 2G2, Canada

²⁴Technische Universität Dresden, Faculty of Chemistry and Food Chemistry, Dresden, 01062, Germany

²⁵Brookhaven National Laboratory, Chemistry Department,

Building 555, P.O. Box 5000, Upton, New York 11973-500, USA

²⁶MTA Atomki, 4001 Debrecen, Hungary

(Dated: June 29, 2022)

This paper reports results from a search for single and multinucleon disappearance from the ^{16}O nucleus in water within the SNO+ detector using all of the available data. These so-called “invisible” decays do not directly deposit energy within the detector but are instead detected through their subsequent nuclear deexcitation and gamma-ray emission. New limits are given for the partial lifetimes: $\tau(n \rightarrow inv) > 9.0 \times 10^{29}$ years, $\tau(p \rightarrow inv) > 9.6 \times 10^{29}$ years, $\tau(nn \rightarrow inv) > 1.5 \times 10^{28}$ years, $\tau(np \rightarrow inv) > 6.0 \times 10^{28}$ years, and $\tau(pp \rightarrow inv) > 1.1 \times 10^{29}$ years at 90% Bayesian credibility level (with a prior uniform in rate). All but the $(nn \rightarrow inv)$ results improve on existing limits by a factor of about 3.

PACS numbers: 11.30.Fs, 12.20.Fv, 13.30.Ce, 14.20.Dh, 29.40.Ka

I. INTRODUCTION

Baryon number and lepton number are accidental symmetries of the Standard Model, yet to date no process violating baryon number and/or lepton number conservation has been observed. Any proven violation of the baryon number conservation principle would be an important step toward explaining the apparent matter-antimatter asymmetry of the Universe. The decay of nucleons would provide a direct observation of baryon number conservation violation and has been the goal of many experiments for the past several decades [1–3]. The particulars of the possible decay modes and their various branching ratios depend heavily on the chosen model, so we seek to make a model-independent measurement of the partial lifetime through individual decay modes. So-called “invisible” decay modes are those where the decay daughter particles cannot be directly observed, but the nuclei are left in an excited state whose deexcitation does deposit energy into the detector. In water, this signal manifests from the energy deposited by gamma-rays in the 5–10 MeV energy window, to which the SNO+ detector is particularly sensitive, owing to its low backgrounds. The decay modes of interest include the disappearance of a single nucleon (n or p) as well as the simultaneous disappearance of a pair of nucleons (nn , np , or pp). Previous limits have been set by SNO [4], KamLAND [5], and SNO+ [6], and this paper presents improved results on those previously published using additional data, reduced background, and improved analysis techniques.

II. THE SNO+ DETECTOR

The SNO+ detector is located underground in Sudbury, Ontario, at a depth of 2070 meters. The detector, which is currently filled with liquid scintillator, had about 1kT target volume of ultrapure water in its first phase of data-taking. This target volume was contained in a 6-meter radius spherical acrylic vessel (AV), which was surrounded by an additional buffer volume of ultrapure water and 9394 8-inch photomultiplier tubes (PMTs) mounted on a steel support structure 9-meters from the center of the AV. The AV is held in suspension through a network of Tensylon ropes anchored both to the laboratory deck above the AV and to the cavity floor. A 7-meter long, 1.6 meter diameter acrylic tube attached

at the top of the AV extends the active volume up to the laboratory deck, where the water comes into contact with the gas above it.

The first set of published data from the SNO+ water phase spanned various periods of detector and water system commissioning between May 2017 and December 2017, and as a result included variable levels of radon-induced background [6]. The data presented here includes a subset of the previous data, as well as an additional set of low background data that was taken after the installation of an AV cover gas system, between October 2018 and July 2019. Radon and its daughters can be drawn into the target volume both through diffusion and convection from the liquid/gas interface at the top of the detector. The AV cover gas is a sealed system that uses nitrogen gas to protect the volume above the water in the detector against radon, reducing the radon ingress by at least an order of magnitude. Further details on the detector can be found in [7, 8].

III. DATA SELECTION

The water phase of the experiment represents a transitional period in which the detector was commissioned and prepared to be filled with liquid scintillator. During this phase, the background levels fluctuated due to changes in the water processing and recirculation system, and the data was divided into periods of relatively stable background levels. The ingress of radon into the detector produces an inhomogeneous field of background activity within the detector.

In this analysis, the fiducial volumes in the different periods were reoptimized to further suppress this variable background. Since almost all of the transient radon appeared near the top of the detector, this was done by comparing the distribution of events in an energy side-band sensitive to radon (4–5 MeV) between the upper and lower hemispheres to estimate the population of events related to transient radon distributions in different fiducial volumes. The fiducial volume was then optimized by balancing the statistical uncertainty and the systematic uncertainty related to the residual transient radon events in the fiducial volume. The previously published data consisted of six distinct sets of data, each with their own selected fiducial volumes. In all cases, the new fiducial volume is smaller than the previous one, and one of

the datasets was removed entirely for this analysis [6]. A breakdown of the individual dataset livetimes and their fiducial volumes is given in Table I. The total livetime across all time periods is 274.7 ± 1.0 days.

IV. EVENT RECONSTRUCTION

Detailed optical calibrations of the detector were carried out, and an updated optical model including a new tabulation of the optical attenuation lengths of the AV and water volumes, was developed and applied to the new dataset, details of the calibration process and comparison with the ^{16}N calibration source can be found in [8]. Additionally, the collective angular response of the PMTs and light concentrators was updated following improved calibrations. This new modeling was only applied to the newly acquired period 6 data and associated simulations, resulting in different reconstruction systematic uncertainties for the old and new data.

Event reconstruction does not differ greatly from the previous results, and involves reconstructing the most likely position (\vec{R}), direction (\vec{U} , orientation of the momentum vector), and effective electron-equivalent kinetic energy (T_e) of an event in the detector based on the arrival time of photons at the PMTs, assuming those photons to be electron generated Cherenkov light. Two additional quantities, the in-time-ratio (ITR) and the light isotropy β_{14} , were used to help identify poor fits and nonphysical events (such as those caused by the detector electronics). These two are as previously described in [6] and the same selection criteria of $\text{ITR} > 0.55$ and $-0.12 < \beta_{14} < 0.95$ in [6] are retained for this analysis. Additionally, several new reconstruction figures of merit were used to identify poorly reconstructed event positions and energies.

Systematic uncertainties arising from the detector modeling and event reconstruction were evaluated using ^{16}N calibration data. Changes in the optical calibration between the previous dataset (periods 1 through 5) and the newest dataset (period 6) require evaluation of that calibration data using the two different models. The improved optical modelling used in the newer dataset improved the energy scale and resolution uncertainty by a factor of 2. Additionally, the uncertainty in the calibration source position was applied as an offset in the newer dataset as opposed to folding it in with the overall position scale uncertainty.

A summary of all of the systematic uncertainties, split by data-taking period, is given in Table II.

V. BACKGROUND MODEL

For each of the hypothetical decay modes considered here, the primary detector signature would be one or more gammas depositing a characteristic quantity of energy. In order to identify such events, it is necessary

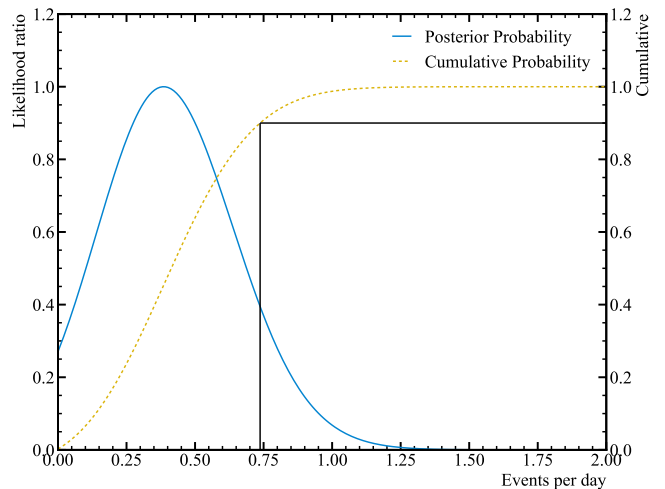


FIG. 1: The likelihood ratio for the neutron decay mode versus the limit of the number of signal decays per day. The associated cumulative distribution indicates the point at which the limit on the signal at 90% C.I. is drawn.

to understand (and thereby account for) various sources of background within the chosen energy window (5–10 MeV).

A. Instrumental background

Low-level data checks were performed to identify and remove spurious events due to instrumentation and other non-physics sources. These data-cleaning cuts entail a small signal sacrifice and an associated contamination that must be taken into account. The signal sacrifice was determined using the ^{16}N calibration source for each dataset, and varies due to the different fiducial volumes. Residual contamination was estimated using a data-driven analysis which compared two sets of data-cleaning cuts using a bifurcated analysis technique. In this technique, the data was separated into 4 categories based on whether it passed or failed two branches of data-cleaning. One branch consisted of a set of low-level data-cleaning cuts based on the hit-times and charge recorded for an event, while the other used the reconstruction classifiers (β_{14} and ITR). Based on the individual leakage of these two branches the resulting sacrifice and contamination for each of the datasets is given in Table III. The estimated contamination and sacrifice are consistent with previous estimates using this technique [6].

B. Cosmogenic background

The depth of the SNO+ detector reduces the total muon flux in the detector to only about 3 muons per

Observable	Period 1	Period 2	Period 3	Period 4	Period 5	Period 6
R (m) max	5.1	5.1	5.1	5.1	5.4	5.2
Z (m) [min, max]	[-6.0, 1.5]	[-6.0, 1.5]	[-6.0, 1.5]	[-3.1, 1.9]	[-6.0, 2.0]	[-6.0, 3.0]
Livetime (days)	5.0	14.6	30.2	28.9	11.2	184.8

TABLE I: Optimized fiducial volume and livetime for each of the included datasets.

Parameter	Uncertainty (1 - 5)	Uncertainty (6)
x offset (mm)	+16.4 -18.2	+50.1 -55.6
y offset (mm)	+22.3 -19.2	+47.7 -59.6
z offset (mm)	+38.4 -16.7	+75.8 -34.7
x scale (%)	+0.91 -1.01	$(x > 0)$ +0.16 -0.23 $(x < 0)$ +0.17 -0.30
y scale (%)	+0.92 -1.02	$(y > 0)$ +0.12 -0.22 $(y < 0)$ +0.17 -0.45
z scale (%)	+0.91 -0.99	$(z > 0)$ +0.30 -0.42 $(z < 0)$ +0.09 -0.24
x resolution (mm)	104	$\sqrt{3214 + 0.393x - 290 }$
y resolution (mm)	98	$\sqrt{2004 + 0.809y - 1365 }$
z resolution (mm)	106	$\sqrt{7230 + 0.730z + 3211 }$
Angular resolution	+0.13 -0.08	+0.122 -0.020
β_{14}	+0.003 -0.010	+0.005 -0.010
Energy scale (%)	2.0	1.02
Energy resolution	+0.018 -0.016	+0.0084 -0.0079

TABLE II: Summary of the evaluated systematic uncertainties for the reconstructed parameters, for the various datasets. Due to updates in the optical modeling, the final dataset (6) has a separate evaluation of these uncertainties from the previous datasets (1 - 5)[6].

Data set	Sacrifice	Contamination (events)
1	$(1.2 \pm 0.3)\%$	0.01 ± 0.02
2	$(1.2 \pm 0.3)\%$	0.04 ± 0.03
3	$(1.2 \pm 0.3)\%$	0.03 ± 0.03
4	$(1.2 \pm 0.3)\%$	0.08 ± 0.06
5	$(1.3 \pm 0.3)\%$	0.01 ± 0.01
6	$(1.7 \pm 0.4)\%$	0.04 ± 0.01

TABLE III: Fraction of signal sacrificed by data-cleaning cuts and the corresponding number of nonphysical events expected to pass the signal selection criteria, as evaluated from the physics data and calibration data.

hour. This is a vital advantage in the search for invisible nucleon decay, since muon spallation reactions producing ^{16}N yield an event signature that is almost identical to the nucleon decay signal. Therefore, it is important to remove the remaining cosmogenic ^{16}N events by muon identification and a 20-second cut on events after each detected muon. Based on an estimated cosmogenic rate from [9, 10], scaled to the SNO+ detector depth, and the 20-second muon veto cut, there is 1 event expected within

the fiducial volume, across the cumulative livetime of the datasets.

C. Radioactive background

The dominant background in this analysis is due to trace levels of residual contamination from uranium and thorium, as well as radon ingress, that primarily manifest as ^{214}Bi and ^{208}Tl decays. The majority of these events fall below the 5-MeV analysis threshold.

The radioactivity intrinsic to the internal water was fit as two individual components, ^{214}Bi and ^{208}Tl . The presence of the AV cover-gas system reduced the internal ^{214}Bi (U-chain) and ^{208}Tl (Th-chain) levels by one order of magnitude compared to the previous analysis [6], with current values of $(5.78 \pm 0.7_{-1.3}^{+1.5}) \times 10^{-15}$ gU/g and $< 4.8 \times 10^{-16}$ gTh/g (95% C.L.), respectively.

For this analysis, all of the decays external to the target volume were treated as a single parameter in the fit. This single parameter includes contributions from decays in the external water, the AV, and the ropes that hold the AV in place. Glass in the PMTs has higher radioactivity relative to other detector components, but the approxi-

mately two and a half meters of external water between the PMTs and the fiducial volume attenuates this contribution to detector background to a negligible level, and so this background was not included in the fit.

D. Neutrino background

Several sources of neutrino and antineutrino background were present, which were constrained through previous experimental results and data. The most significant source of background comes from ^8B solar neutrinos, which have been well measured. For these results, the solar neutrino flux is constrained based on recent results from Super-Kamiokande [11], which are consistent with both the SNO [12] and SNO+ [13] measurements, with oscillations applied using the BS2005-OP solar model [14].

Atmospheric neutrino interactions also create signals within the detector through neutral current interactions that can liberate nucleons from the oxygen nucleus. The subsequent deexcitation of $^{15}\text{N}^*$ or $^{15}\text{O}^*$ could look identical to the single proton and neutron decay modes. However, many of these interactions can be identified by detecting the neutron captures that follow the event. Estimates based on GENIE simulations [15] predict about 0.1 interactions produce an excited state nucleus per day within the entire internal water volume. By including the uncertainty on the atmospheric neutrino flux, GENIE branching ratio, and the interaction cross-section, a 67% total uncertainty on the normalization of the atmospheric contamination rate was found.

Antineutrinos from the nearby nuclear reactors were also considered in the analysis, though their overall contribution was relatively small. The flux estimates combined reactor information from the International Atomic Energy Agency [16] with Canadian reactor power information [17] to provide a constraint. Furthermore, because the reactor signals are inverse beta decays, the neutron follower cut designed to reduce the number of atmospheric events served to also reduce the reactor antineutrino background. The total number of reactor antineutrino background events was fit in the analysis with the included constraint from the flux, yielding an estimate of 1.8 events summed across all of the datasets within the fiducial volumes.

E. Additional subdominant backgrounds

Other backgrounds were studied and found to be negligible in magnitude and not included in the fit. These backgrounds would not normally fall within the region of interest, but can occasionally do so due to misreconstruction. From Monte Carlo simulations, the PMT background is expected to contribute fewer than 0.1 events within the region of interest in the entire dataset. The other considered sources of subdominant background

were (α, n) reactions on ^{13}C (acrylic) or ^{18}O (acrylic and water) nuclei. In the ^{13}C case, an α is captured on the nucleus, resulting in a neutron and a ^{16}O nucleus, which can be produced in an excited state of 6.1 MeV up to 10% of the time. The gammas or electrons/positrons emitted in the deexcitation have a small chance of falling into the region of interest (ROI) for this study. However, the reaction on ^{18}O produces low energy gammas and, therefore, it is expected to make a negligible contribution in the ROI. The dominant source of alphas is from ^{210}Po embedded a few nanometers below the AV surface [7].

In total, there are expected to be fewer than 1.4 events out of a total of 239 in the dataset that are not included in the fit. The expected contribution from these backgrounds are not subtracted from the final signal count, producing a more conservative upper limit on the nucleon decay lifetimes.

VI. ANALYSIS METHODS

This analysis applied new selection criteria to the previous data (consisting of datasets 1 through 5), with the addition of the sixth blinded dataset. Data was blinded in the approximate energy range of 5 to 15 MeV based on the number of PMT hits per event. The region outside of the blinded region (unblinded data) was used for a fiducial volume selection study. As a result of radon ingress from the gas/liquid interface above, the spatial field of background radioactivity in the detector was not homogeneous, and so it was necessary to limit the fiducial volume by placing a varying cut in Z for each of the datasets independently. Since these asymmetries are not modeled in Monte Carlo simulations, an analysis on data outside of the region of interest, from 4–5 MeV, was used to assess this top-bottom asymmetry and select a fiducial volume that would minimize the uncertainty due to this event contamination. The event selection criteria for each of the individual datasets is given in Table I. After applying the selection criteria and each decay mode's individual branching ratio, the final signal acceptance efficiencies are given in Table IV.

Events within the selected ROI between 5 and 10 MeV were fitted using an unbinned maximum likelihood method with probability distributions produced from the Monte Carlo in energy, position, and direction. The normalization on the signal rate and the rate of internal and external radioactive backgrounds were fit unconstrained, while the cosmogenic ^{16}N , atmospheric neutrino, and solar neutrino events included a Gaussian constraint as discussed in the previous section. The fitting technique was repeated for each of the signals of interest (n , p , pp , np , and nn decay) independently. The Monte Carlo model simulates events uniformly in time throughout the data taking window, including variations in the detector state. The probability distribution functions (PDFs) were separated into a one-dimensional distribution in R^3 multiplied by a two-dimensional distribution in $(\cos\theta_{\text{sun}}, T_e)$,

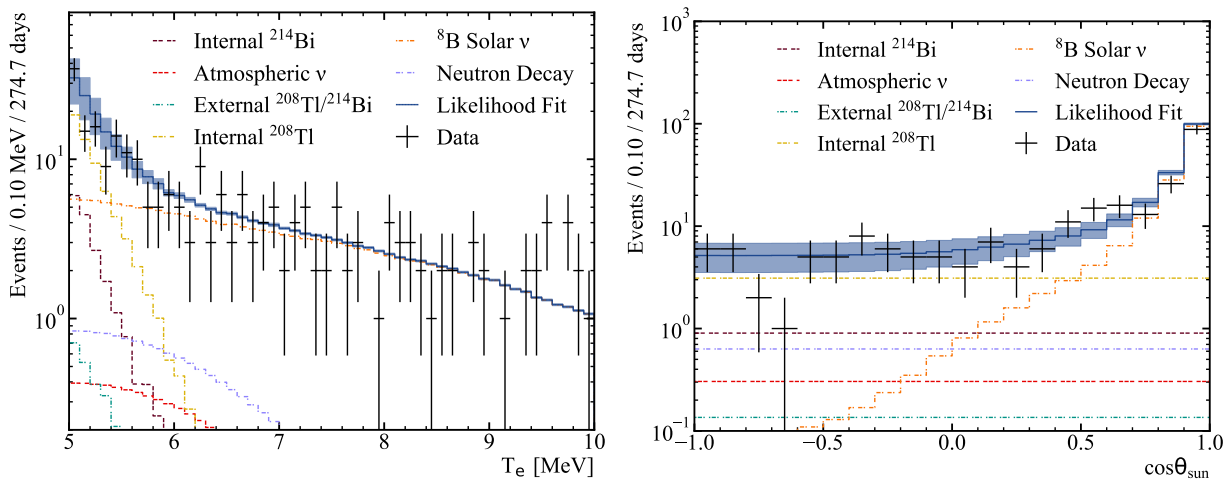


FIG. 2: Projection of the reconstructed energy (left) and the dot product of the reconstructed direction and the solar direction (right) for the entire dataset. The error bands on the total fit show the result of all of the systematic uncertainties applied. The neutron decay signal shown is at the best-fit lifetime of 1.7×10^{30} years.

where $\cos\theta_{\text{sun}}$ is the dot product between the reconstructed event direction and the position of the sun with respect to the event position. The choice to split the full PDF this way was due to the strong correlation between $\cos\theta_{\text{sun}}$ and T_e found in the solar neutrino background (due to the decreasing opening angle between the electron and the incident neutrino in the elastic scattering process), and the relatively weak correlation with respect to position.

To evaluate the effect of the systematic uncertainties on the reconstructed parameters, the probability distributions for each signal and background were reconstructed with each parameter varied by one standard deviation in each direction as given in Table II. The full data was then refitted with each of the new sets of PDFs, and the difference between the new best-fit signal and the nominal best-fit taken as the systematic uncertainty on the number of signal counts. The nominal likelihood function was then convolved with an asymmetric normal distribution, whose width was determined by the quadrature sum of these systematic uncertainties. The signal upper limit is then determined by directly integrating the likelihood function, with a positive uniform prior in rate, up to the 90% interval.

VII. RESULTS

Results for the upper limit on the five decay modes of interest, including systematic uncertainties, are evaluated independently and given in Table V. The total T_e and $\cos\theta_{\text{sun}}$ spectra for the combined dataset for the neutron decay mode are shown in Fig. 2, where the bands on the total spectrum show the effect that the systematic uncertainties have on the final spectral shape. The signal likelihood is shown in Fig. 1, which in each of the studied

Data Set	Signal Efficiency (%)				
	n	p	pp	np	nn
1	$11.4^{+0.7}_{-0.7}$	$13.2^{+0.7}_{-0.7}$	$11.5^{+0.5}_{-0.5}$	$6.6^{+0.3}_{-0.3}$	$1.84^{+0.07}_{-0.06}$
2	$11.6^{+0.7}_{-0.7}$	$13.3^{+0.7}_{-0.7}$	$11.5^{+0.5}_{-0.5}$	$6.6^{+0.3}_{-0.3}$	$1.84^{+0.07}_{-0.06}$
3	$11.5^{+0.7}_{-0.7}$	$13.3^{+0.7}_{-0.7}$	$11.5^{+0.5}_{-0.5}$	$6.6^{+0.3}_{-0.3}$	$1.84^{+0.07}_{-0.06}$
4	$10.9^{+0.7}_{-0.6}$	$12.6^{+0.6}_{-0.6}$	$10.8^{+0.5}_{-0.5}$	$6.2^{+0.3}_{-0.3}$	$1.72^{+0.07}_{-0.05}$
5	$14.6^{+0.9}_{-0.8}$	$16.8^{+0.8}_{-0.8}$	$14.4^{+0.6}_{-0.6}$	$8.3^{+0.4}_{-0.4}$	$2.31^{+0.09}_{-0.07}$
6	$13.9^{+0.4}_{-0.4}$	$16.4^{+0.4}_{-0.4}$	$14.2^{+0.3}_{-0.3}$	$8.2^{+0.2}_{-0.2}$	$2.38^{+0.04}_{-0.02}$

TABLE IV: The acceptance efficiency of the signal after applying analysis cuts and the individual nuclear branching ratios. The reconstruction systematic uncertainties are given alongside each efficiency.

Decay Mode	Partial Lifetime Limit	Existing Limits
n	9.0×10^{29} y	5.8×10^{29} y [5]
p	9.6×10^{29} y	3.6×10^{29} y [6]
pp	1.1×10^{29} y	4.7×10^{28} y [6]
np	6.0×10^{28} y	2.6×10^{28} y [6]
nn	1.5×10^{28} y	1.4×10^{30} y [5]

TABLE V: Lifetime limits at 90% C.I. for the invisible decay modes of interest alongside the existing limits.

decay modes is consistent with no observed signal.

VIII. CONCLUSION

Multiple datasets totaling 274.7 days of data-taking were analyzed to search for five selected modes of “invisible” nucleon decay (n , p , nn , pp , np). Results are consistent with no observation of invisible nucleon decay for all

the studied decay modes, and represent an improvement on previous limits for all but the nn decay mode. In particular, the addition of the longer low-background data set improved the previous SNO+ results on the n and p decay modes by a factor of 3 while improving the np and pp decay modes by a factor of 2 [6]. The much smaller improvement found in the nn decay mode was investigated and found to be due to its energy spectrum. Compared with the other four modes, the cascade of gamma-rays from nn extends out to higher energies, making the signal less distinguishable from ${}^8\text{B}$ solar neutrino events. As can be seen in Fig. 2, the large number of events at high energy, and the slight deficit of events in the solar direction lowers the sensitivity to the nn decay mode.

ACKNOWLEDGMENTS

Capital construction funds for the SNO+ experiment were provided by the Canada Foundation for Innovation (CFI) and matching partners. This research was supported by: **Canada:** Natural Sciences and Engineering Research Council, the Canadian Institute for Advanced Research (CIFAR), Queen’s University at Kingston, Ontario Ministry of Research, Innovation and Science, Alberta Science and Research Investments Program, Federal Economic Development Initiative for Northern Ontario, Ontario Early Researcher Awards; **U.S.:** Department of Energy Office of Nuclear Physics, National Science Foundation, Department of Energy National Nuclear Security Administration through the Nuclear Science and Security Consortium; **UK:** Science and Technology Facilities Council (STFC), the European Union’s Seventh Framework Programme under the European Research Council (ERC) grant agreement, the Marie Curie grant agreement; **Portugal:** Fundação para a Ciência e

a Tecnologia (FCT-Portugal); **Germany:** the Deutsche Forschungsgemeinschaft; **Mexico:** DGAPA-UNAM and Consejo Nacional de Ciencia y Tecnología.

We thank the SNO+ technical staff for their strong contributions. We would like to thank SNOLAB and its staff for support through underground space, logistical and technical services. SNOLAB operations are supported by CFI and the Province of Ontario Ministry of Research and Innovation, with underground access provided by Vale at the Creighton mine site.

This research was enabled in part by support provided by WestGRID (www.westgrid.ca) and Compute Canada (www.computeCanada.ca) in particular computer systems and support from the University of Alberta (www.ualberta.ca) and from Simon Fraser University (www.sfu.ca) and by the GridPP Collaboration, in particular computer systems and support from Rutherford Appleton Laboratory [18, 19]. Additional high-performance computing was provided through the “Illumine” cluster funded by CFI and Alberta Economic Development and Trade (EDT) and operated by ComputeCanada and the Savio computational cluster resource provided by the Berkeley Research Computing program at the University of California, Berkeley (supported by the UC Berkeley Chancellor, Vice Chancellor for Research, and Chief Information Officer). Additional long-term storage was provided by the Fermilab Scientific Computing Division. Fermilab is managed by Fermi Research Alliance, LLC (FRA) under Contract with the U.S. Department of Energy, Office of Science, Office of High Energy Physics.

For the purposes of open access, the authors have applied a Creative Commons Attribution licence to any Author Accepted Manuscript version arising. Representations of the data relevant to the conclusions drawn here are provided within this paper.

-
- [1] K. Abe *et al.* (Super-Kamiokande), Phys. Rev. D **95**, 012004 (2017).
 - [2] K. Abe *et al.* (Super-Kamiokande), Phys. Rev. D **96**, 012003 (2017).
 - [3] K. Abe *et al.* (Super-Kamiokande), arXiv:1811.12430.
 - [4] S. Ahmed *et al.* (SNO), Phys. Rev. Lett. **92**, 102004 (2004).
 - [5] T. Araki *et al.* (KamLAND), Phys. Rev. Lett **96**, 101802 (2006).
 - [6] M. Anderson *et al.* (SNO+), Phys. Rev. D **99**, 032008 (2019), arXiv:1812.05552 [hep-ex].
 - [7] V. Albanese *et al.* (SNO+), JINST **16**, P08059 (2021), arXiv:2104.11687 [physics.ins-det].
 - [8] M. Anderson *et al.* (SNO+), JINST **16**, P10021 (2021).
 - [9] S. W. Li and J. F. Beacom, Phys. Rev. C **89**, 045801 (2014).
 - [10] Y. Zhang *et al.* (Super-Kamiokande Collaboration), Phys. Rev. D **93**, 012004 (2016).
 - [11] K. Abe *et al.* (Super-Kamiokande), Phys. Rev. D **94**, 052010 (2016).
 - [12] B. Aharmim *et al.* (SNO Collaboration), Phys. Rev. C **88**, 025501 (2013).
 - [13] M. Anderson *et al.* (SNO+ Collaboration), Phys. Rev. D **99**, 012012 (2019).
 - [14] J. Bahcall *et al.*, ApJ **621** (2005).
 - [15] C. Andreopoulos *et al.*, Nucl. Instrum. Meth. A **614**, 87 (2010), arXiv:0905.2517 [hep-ph].
 - [16] IAEA (International Atomic Energy Agency), “Power reactor information system,” <https://pris.iaea.org/PRIS/home.aspx>.
 - [17] IESO (Independent Electricity System Operator), “Power data,” <https://ieso.ca>.
 - [18] P. J. W. Faulkner *et al.* (The GridPP collaboration), Journal of Physics G: Nuclear and Particle Physics **32**, N1 (2006).
 - [19] D. Britton *et al.* (The GridPP collaboration), Philosophical Transactions of the Royal Society of London A: Mathematical, Physical and Engineering Sciences **367**, 2447 (2009).